Biosensors and Bioelectronics 142 (2019) 111536

Contents lists available at ScienceDirect

Biosensors and Bioelectronics

journal homepage: www.elsevier.com/locate/bios

Construction of Tb-MOF-on-Fe-MOF conjugate as a novel platform for ultrasensitive detection of carbohydrate antigen 125 and living cancer cells

Minghua Wang, Mengyao Hu, Zhenzhen Li, Linghao He, Yingpan Song, Qiaojuan Jia, Zhihong Zhang*, Miao Du**

Henan Provincial Key Laboratory of Surface and Interface Science, Zhengzhou University of Light Industry, Zhengzhou, 450002, PR China

ARTICLE INFO

Keywords:
Impedimetric aptasensor
MOF-On-MOF
TbFe-MOFs
CA125
MCF-7

ABSTRACT

Combining different metal−organic frameworks (MOFs) into a conjugate material can integrate the properties of each MOF component and further lead to emergent properties from the synergistic heterostructured units. In this work, two kinds of bimetallic TbFe-MOFs have been designed by MOF-on-MOF strategy and utilized as a platform for anchoring carbohydrate antigen 125 (CA125) aptamer to detect CA125 and living michigan cancer foundation-7 (MCF-7) cells. Although the integrated MOF-on-MOF architectures show similar chemical and structural features to that of the top layer, the Fe-MOF-on-Tb-MOF and Tb-MOF-on-Fe-MOF have different surface nanostructures to their parent MOFs. The developed aptasensor based on Tb-MOF-on-Fe-MOF displays higher stability of the formed G-quadruplex between aptamer and CA125 than that based on Fe-MOF-on-Tb-MOF, owing to stronger immobilization behavior of the aptamer for the Tb-MOF-on-Fe-MOF composite. The developed aptasensor provides an extremely low detection limit of 58 $\mu U \cdot mL^{-1}$ towards CA125 within a wide linear range from 100 $\mu U \cdot mL^{-1}$ to 200 $U \cdot mL^{-1}$, which is significantly lower than those of all reported sensors. This aptasensor also has high selectivity, good stability, acceptable reproducibility, and excellent applicability in human serum. Moreover, the Tb-MOF-on-Fe-MOF nanoarchitecture demonstrates superior biocompatibility and good endocytosis. As a result, the developed aptasensor illustrates high sensitivity for detection of MCF-7 cells with an extremely low detection limit of 19 $cell \cdot mL^{-1}$. Therefore, the proposed aptasensor based on Tb-MOF-on-Fe-MOF exhibits great potentials for early diagnosis of tumors.

1. Introduction

Aptamers with 25 to 90 bases in length can be obtained via systematic evolution of ligands by exponential enrichment (Mendonsa and Bowser, 2005), which show high specificity and binding affinity to different target molecules. Typical structural motifs of aptamers include stems, internal loops, purine-rich bulges, hairpins, pseudoknots, kissing complexes, and G-quadruplexes (Stoltenburg et al., 2007). Most aptamers can bind to their respective targets through the complementary shape interactions and 3D folding with high affinity and specificity (Meng et al., 2016). Compared with antibodies, aptamers have higher specificity of binding affinity, sufficient stability, resistance to harsh environments, smaller sizes, and higher purity (Trausch et al., 2017). Hence, aptamers have been considered as promising alternatives for antibodies in biosensing devices. Various techniques, such as fluorescence spectroscopy, surface plasmon resonance (SPR) (Gedi et al., 2018), colorimetric approach (Wei et al., 2007), and electrochemical methods (Jalalian et al., 2018), have been employed to develop different aptamer sensors (aptasensors) for detection of target analytes. In this context, electrochemical aptasensors combine the individual features of electrochemical methods and have been widely applied because of their small size, low cost, high efficiency, ease of operation, high selectivity, and sensitivity (Taghdisi et al., 2016). Electrochemical impedance spectroscopy (EIS) is an effective technique to demonstrate the formation of complexes between biomolecules immobilized on an electrode surface by probing the electrode/electrolyte interface, which is generally used to develop aptasensors towards diverse cancer markers (Törer et al., 2018). A typical electrochemical biosensor system mainly consists of biorecognition element and signal transducer, including a modified layer, an electrode substrate and an electronic detection system. Normally, the organic molecules and nanomaterials, such as carbon nanomaterials (Deng et al., 2018), quantum dots, polymeric films (Deng et al., 2017), and organic nanoparticles (NPs), serve as the support materials that link the aptamer probes to substrates

* Corresponding author.
** Corresponding author.
E-mail addresses: 2006025@zzuli.edu.cn (Z. Zhang), dumiao@zzuli.edu.cn (M. Du).

https://doi.org/10.1016/j.bios.2019.111536
Received 6 May 2019; Received in revised form 10 July 2019; Accepted 24 July 2019
Available online 25 July 2019
0956-5663/

(He and Tian, 2016). However, these nanomaterials possess few anchoring sites and low detection sensitivity for the lack of chemical functionality, small specific surface areas, and fussy preparation (Xu et al., 2017). In this connection, it is of great challenge to develop advanced nanomaterials as transducers of electrochemical aptasensors to enhance their sensing performances.

Metal–organic frameworks (MOFs), constructed by coordination bonds between metal ions and organic ligands, are promising materials because of their porous crystalline structures, abundant compositions, and easy preparation (Du et al., 2013; Yin et al., 2019). MOFs exhibit interesting properties and significant applications in a variety of fields, such as gas storage or separation, catalysis, energy conversion, sensors, and biomedical diagnosis (Chang et al., 2015). However, the application of MOFs in electrochemical aspect is limited due to their inherent drawbacks, including poor electron transfer capability and unsteadiness in water environments (Qiao et al., 2019). Porous MOFs are considered as ideal candidates that may immobilize DNA or aptamers due to their excellent adsorption capacities and tailored grafting groups such as $–NH_2$ or –COOH (Liu et al., 2017; Li et al., 2018b). Various MOF-based aptasensors have been developed for detection of antibiotics, cancer markers, and heavy metal ions (Lu et al., 2019; Wang et al., 2019; Zhou et al., 2019). Moreover, incorporating MOFs with other functional species (e.g. NPs, biomolecules, nanofibers or polymers) can functionalize bulk MOFs with improved properties compared with their pristine counterparts, considering the distinct features of MOFs such as highly diversified structures, large surface areas, tunable pores, and customizable chemistry (Li and Huo, 2015). The conjugation of MOFs with other materials is a significant route to extend the applications of MOFs in sensing fields. For instance, MOFs can be combined with covalent–organic frameworks to fabricate electrochemical aptasensors for antibiotics detection (Liu et al., 2019; Zhou et al., 2019). Au NPs (Su et al., 2017), Ag nanoclusters (Guo et al., 2017; Lee et al., 2018), and Pt NPs (Li et al., 2018a) are embedded within MOFs as scaffolds for aptasensors.

Heterostructured MOFs have received increasing interest owing to the integrated properties from each MOF component and the emergent properties from the synergistic heterostructured units (Wang et al., 2018a). Combining diverse MOFs into a hybrid system can be employed to develop modular devices with multiple properties, such as united catalysis, purification or enhanced sorption, and separation capacity (Feng et al., 2018). For example, the isotropic growth of MIL-68-Br on MIL-68 template results in core-shell MIL-68@MIL-68-Br (Choi et al., 2016). MIL-101(Cr)@NH_2-MIL-125(Ti) exhibits high efficiency in the adsorption-photocatalytic removal of Cr(VI) due to the synergies between MIL-101(Cr) and NH_2-MIL-125(Ti) in this core-satellite hetero-architecture (Gu et al., 2017). NH_2-MIL-101(Al)@ZIF-8 is successfully fabricated as a versatile material for the efficient adsorption and sensitive detection of Cu(II) in water (Zhang et al., 2018a). A facile one-pot ion modulation strategy is explored to construct core-shell MOF@MOF, which enables the shape control of Mn-MOF@Fe-MOF with diverse morphologies at room temperature (Wu et al., 2018). Very recently, two novel bimetallic ZnZr-based MOFs via MOF-on-MOF method have been prepared and used as scaffold substrates for aptasensors to achieve sensitive detection of protein tyrosine kinase 7 (Zhou et al., 2019). Also, the bimetallic ZrHf-MOF has been employed as the platform for determination of human epidermal growth factor receptor-2 (HER2) and living cancer cells (Gu et al., 2019). However, the rational design of MOF-on-MOF or core-shell MOFs for biosensing applications is still in early stage.

Fe(III)-based MOFs (Fe-MOFs) or Fe-MOF-derived nanomaterials usually show excellent stability, redox activity, and good sensing performances when used as electrode materials (Alizadeh et al., 2017; Liu et al., 2018; Song et al., 2017). In addition, Ln-MOFs, especially those with europium and terbium as metal nodes, display unique luminescent properties, such as large Stokes shift, bright visible emission, long decay lifetime and undisturbed emissive energy. A nanocomposite of Tb-MOF and Au NPs is established as the scaffold of aptasensor for quantification determination of adenosine triphosphate (Qu et al., 2018). Considering the remarkable sensing performances, high electrochemical activity, and excellent biocompatibility of Fe-MOF and Tb-MOF as well as fluorescence of Tb-MOF, the heterostructured bimetallic TbFe-MOF can be constructed and applied as a new platform to anchor the aptamer strands for simultaneously detecting cancer markers and living cancer cells.

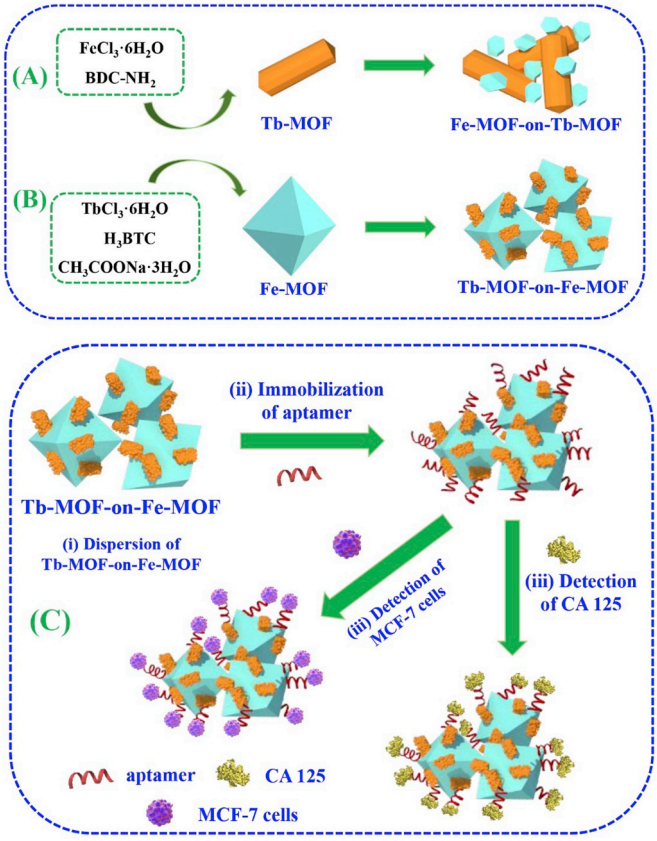

Scheme 1. Schematic diagram of the preparation of **(A)** Fe-MOF-on-Tb-MOF and **(B)** Tb-MOF-on-Fe-MOF nanostructures and **(C)** the fabrication procedure of aptasensor based on two kinds of TbFe-MOFs (taking Tb-MOF-on-Fe-MOF-based aptasensor as an example), including (i) dispersion of Tb-MOF-on-Fe-MOF, (ii) aptamer immobilization and (iii) detection of CA125 and living MCF-7 cells.

In current study, we design and prepare two kinds of novel bimetallic core-shell Tb-MOF-on-Fe-MOF and Fe-MOF-on-Tb-MOF nanostructures for the first time with MOF-on-MOF approach, which are employed as transducer materials for aptasensors (Parts **A** and **B**, Scheme 1). Taking the detection of carbohydrate antigen (CA) 125, as an example, a proposed probe is made to immobilize on such bimetallic nanomaterials to sensitively detect CA125 (Part **C**, Scheme 1). CA125, discovered as a cancer antigen in 1983, is regarded as a tumor marker for monitoring the treatment results of patients with ovarian cancer (Cramer et al., 2018). In healthy population, the serum level of CA125 is below 35 $U·mL^{-1}$. The serum levels of CA125 in ovarian epithelial carcinoma are elevated, which are significant in diagnosis, prognosis, disease monitoring, and during follow up of treatment (Razmi and Hasanzadeh, 2018). The entire fabrication of the developed aptasensors is investigated by electrochemical technique due to the substantial change in electrochemical activity of the modified electrode. In comparison, the Tb-MOF-on-Fe-MOF-based aptasensor has superior sensing performance for detection of CA125 than the Fe-MOF-on-Tb-MOF-based aptasensor. The heterostructure of bimetallic TbFe-MOFs can improve the sensing performance by integrating the good

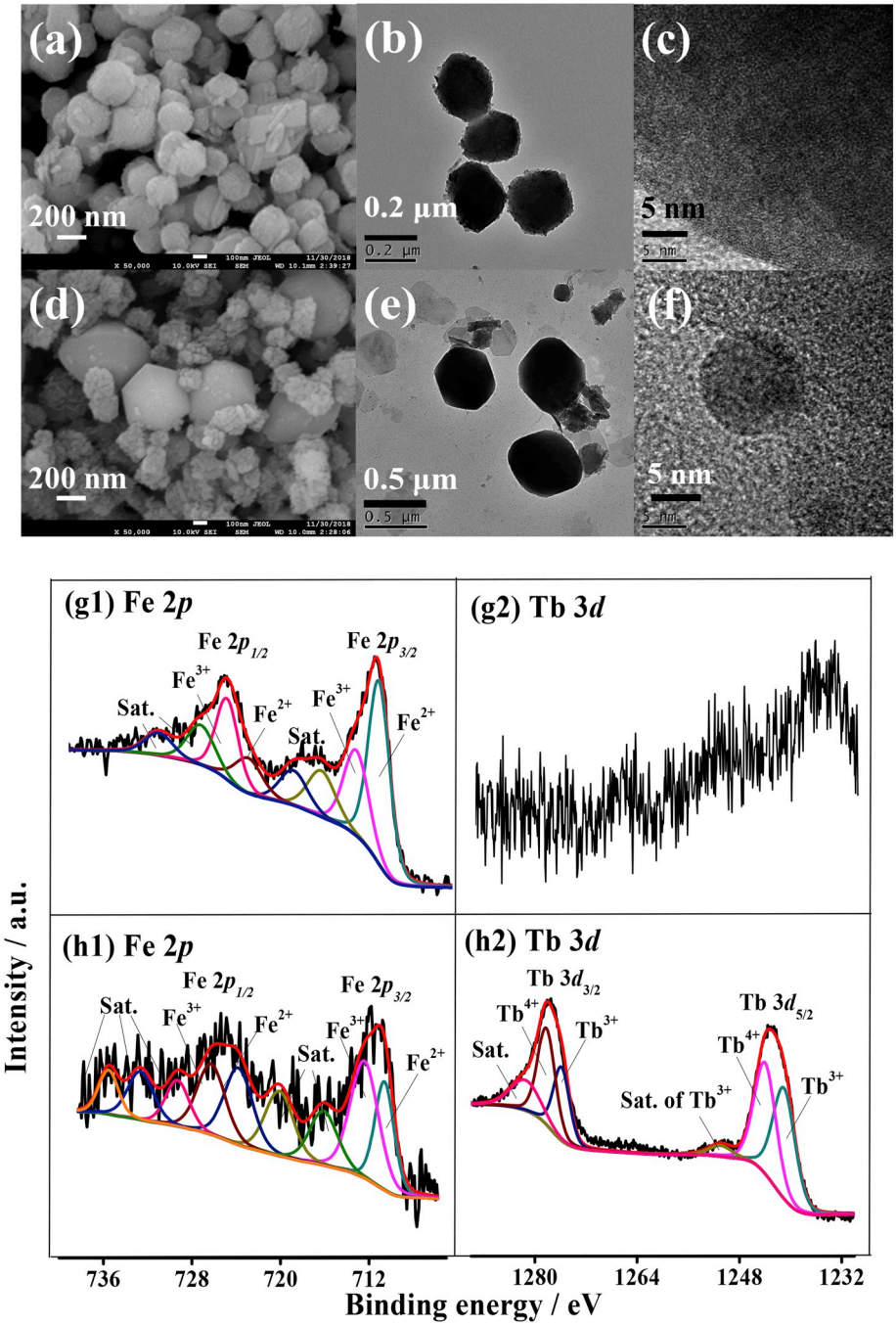

Fig. 1. SEM, TEM and HR-TEM images of (a, b, c) Fe-MOF-on-Tb-MOF and (d, e, f) Tb-MOF-on-Fe-MOF. High-resolution Fe 2*p* and Tb 3*d* XPS spectra of (g) Fe-MOF-on-Tb-MOF and (h) Tb-MOF-on-Fe-MOF.

biocompatibility and strong anchoring ability towards the aptamer strand of Fe-MOF (Zhang et al., 2017) and the high electrochemical activity and fluorescence of Tb-MOF (Qu et al., 2018). Additionally, the Tb-MOF-on-Fe-MOF-based aptasensor can be used to detect the living cancer cells for its biocompatibility and endocytosis.

2. Experimental section

The parts of materials and chemicals, preparation of all solutions, pretreatment of the bare Au electrode (AE), synthesis of Fe- and Tb-MOF, characterizations, electrochemical measurements, and cell culture, cell imaging, and cytotoxicity in vitro were supplied in **Supplementary Material S1.**

2.1. Synthesis of Tb-MOF-on-Fe-MOF and Fe-MOF-on-Tb-MOF nanostructures

In case of Tb-MOF-on-Fe-MOF preparation, the as-obtained Fe-MOF was used as the template. Firstly, the as-prepared Fe-MOF (30 mg) was dispersed into 7 mL of N,N-dimethylformamide (DMF) to form the uniform suspension. Afterward, 209 mg $TbCl_3{\cdot}6H_2O$ was dissolved in DMF/water (v/v = 5/4, 18 mL) to obtain a homogeneous solution. Then, the Fe-MOF suspension and the $TbCl_3$ solution were mixed, followed by adding 42 mg 1,3,5-benzenetricarboxylic acid (H_3BTC) and 108.9 mg anhydrous sodium acetate. Finally, the mixed solution was transferred into a Teflon-lined stainless-steel autoclave (50 mL) and heated at 80 °C for 24 h. The crystalline product was washed with

ethanol for several times, and dried in an oven at 60 °C.

In terms of Fe-MOF-on-Tb-MOF preparation, the as-obtained Tb-MOF (20 mg) was dispersed into 7 mL of DMF to produce a homogeneous dispersion. Subsequently, 337 mg $FeCl_3{\cdot}6H_2O$ was dissolved in 7 mL of DMF. The Tb-MOF dispersion and the $FeCl_3$ solution were mixed, followed by adding 112 mg terephthalic acid (H_2BDC). The resultant solution was transferred into a Teflon-lined stainless-steel autoclave (50 mL) and heated at 110 °C for 24 h. The product was washed with ethanol for several times, and dried in an oven at 60 °C.

2.2. Fabrication of CA125 aptasensors based on MOFs

Taking the development of Tb-MOF-on-Fe-MOF-based aptasensor as an example, the fabrication procedure was shown as below. First, Tb-MOF-on-Fe-MOF (1 mg) composite was dispersed in 1 mL of Milli-Q ultrapure water to afford a homogeneous dispersion with a concentration of 1 mg· mL^{-1}. Then, 5.0 μL of Tb-MOF-on-Fe-MOF suspension was dropped on the pre-treated AE and dried at room temperature for 4 h (represented by Tb-MOF-on-Fe-MOF/AE). Subsequently, Tb-MOF-on-Fe-MOF/AE was immersed in the aptamer solution for 30 min, followed by washing with Milli-Q water thoroughly (represented by Apt/Tb-MOF-on-Fe-MOF/AE).

The dispersions of Fe-MOF, Tb-MOF, and Fe-MOF-on-Tb-MOF were prepared by a similar route as described above. The aptasensors based on Fe-MOF, Tb-MOF, and Fe-MOF-on-Tb-MOF were also fabricated by the same approach to that based on Tb-MOF-on-Fe-MOF. All as-obtained aptasensors were used for further electrochemical measurements and stored in a refrigerator (4 °C) when not use.

2.3. Electrochemical measurements

The as-obtained aptasensors were immersed into the CA125 solution and living MCF-7 cells with various concentrations for electrochemical measurements to determine their limit of detection (LOD). The selectivity of aptasensor was determined by incubation with carbohydrate antigen 19-9 (CA19-9), vascular endothelial growth factor (VEGF), immunoglobulin G (IgG), carcinoembryonic antigen (CEA), mucin 1 (MUC1), epidermal growth factor receptor (EGFR), porcine serum albumin (PSA), and alpha-fetoprotein (AFP) at room temperature. For stability assessment, the aptasensor was stored at 4 °C for 15 days and measured by EIS every day. Human serum was used to verify the applicability of aptasensors, in which the CA125 solution with different concentrations were spiked into the sample, as 500-fold diluted by PBS (0.01 M, pH 7.4). The incubation time with real samples is 60 min for aptasensors.

3. Results and discussion

3.1. Basic characterizations of Fe-MOF-on-Tb-MOF and Tb-MOF-on-Fe-MOF

The morphologies and microstructures of four kinds of MOFs were analyzed by field emission scanning electron microscope (FE-SEM) and transmission electron microscopy (TEM) (Fig. S2, **S3**, and **1**). The details for Fe-MOF and Tb-MOF were shown in **Supplementary Material S2**. As shown in Fig. 1a and b, the Fe-MOF-on-Tb-MOF exhibits ball-like structure with an average size of ca. 300 nm, while no clear lattice fringe is observed in its high resolution TEM (HR-TEM) image (Fig. 1c). The possible reason for this is that the introduction of Fe-MOF precursor and the relatively higher temperature render the structure of Tb-MOF changing from cylindrical to sphere shape. The Tb-MOF conversely confines the growth of Fe-MOF on the Tb-MOF surface, leading to the reduced size of Fe-MOF-on-Tb-MOF as compared with those of the individual Fe-MOF and Tb-MOF. As for the Tb-MOF-on-Fe-MOF, its SEM image (Fig. 1d) shows different morphology of Fe-MOF and Tb-MOF, in which the Fe-MOF displays hexagon structure, while a number of NPs are assembled to form the cylindrical structure of Tb-MOF. Besides, the content of Tb-MOF is higher than that of Fe-MOF, which is also confirmed by X-ray photoelectron spectroscopy (XP) analysis shown as below (Fig. 1h). All results demonstrate that the existence of Fe-MOF has restrictive effect on the synthesis and crystallization behavior of Tb-MOF. Despite the appearance of the clear lattice fringe in the parent Tb-MOF, no lattice fringe is obtained in the HR-TEM image of the Tb-MOF-on-Fe-MOF (Fig. 1f), hinting its low crystallinity. This feature of the Tb-MOF-on-Fe-MOF seems to facilitate biomolecules to anchor (Zhou et al., 2019a).

To confirm the successful synthesis of Fe-MOF, Tb-MOF, Fe-MOF-on-Tb-MOF, and Tb-MOF-on-Fe-MOF, X-ray diffraction (XRD), Fourier transform infrared spectra (FT-IR), XPS, and fluorescence characterizations were carried out (**Supplementary Material S3**). The XRD result of Fe-MOF-on-Tb-MOF was similar to that of Tb-MOF, while the XRD pattern of Tb-MOF-on-Fe-MOF was the same to that of Fe-MOF (Fig. S4a). This condition was because only the surface crystal structures of Fe-MOF-on-Tb-MOF and Tb-MOF-on-Fe-MOF composites were determined due to the thickness limitation of XRD measurements. Furthermore, to investigate the chemical components and environments of Fe and Tb elements contained in Fe-MOF and Tb-MOF, high-resolution XPS spectra of Fe 2*p* and Tb 3*d* were analyzed (Figs. S5 and S6). Fe^{2+} and Fe^{3+} species coexisted in Fe-MOF, along with different organic carbon-related groups, such as C-C, C-O, COO, and π-π* binding, which originated from the organic ligands in MOFs. Meanwhile, Tb^{3+} and Tb^{4+} were both combined in Tb-MOF, with the similar organic functional groups to those of Fe-MOF. With regard to Fe-MOF-on-Tb-MOF, the high-resolution XPS spectrum of Fe 2*p* revealed similar deconvoluted peaks with that of Fe-MOF (Fig. 1g1). However, no substantial Tb 3*d* signal was observed (Fig. 1g2). In fact, only the chemical structure and component of material surface (thickness ≤ 8–10 nm) can be determined through XPS (Aycla et al., 2006). In Fe-MOF-on-Tb-MOF, the Tb-MOF layer was fully covered by the Fe-MOF layer and thus, the Tb signal was not measured. On the contrary, a clear Tb 3*d* signal appeared in Tb-MOF-on-Fe-MOF (Fig. 1h2), in which similar analysis results fitted with that of Tb 3*d* of Tb-MOF. Compared with Fe-MOF-on-Tb-MOF, a weaker Fe 2*p* signal was observed (Fig. 1h1), showing the coexistence of Fe^{2+} and Fe^{3+} ions. In fact, only the structure of nanomaterial surface can be probed through XRD and XPS (Mi et al., 2013). The porous nanostructures and physicochemical properties of bulk materials play an important role in sensing performances. As shown in Fig. S7, Tb-MOF-on-Fe-MOF exhibits four characteristic emission spectra at 489 nm, 544 nm, 584 nm, and 618 nm, respectively. Significantly, the strongest emission peak at 584 nm corresponds to the $^5D_4 \rightarrow {}^7F_4$ transitions for the Tb^{3+} ion, resulting in the bright green light which can be observed by naked eyes. All results indicate that Tb-MOF exhibits unique luminescent property, and also verify the successful formation of Tb-MOF-on-Fe-MOF, which is beneficial for the further cell imaging application.

3.2. Electrochemical sensing performances of developed aptasensors

Considering the basic performance of bimetallic TbFe-MOFs, their electrochemical sensing properties should be assessed when used as the platforms for aptasensors. Here, the as-prepared bimetallic TbFe-MOFs were used as the transducer nanomaterials for anchoring CA125 aptamer and detecting CA125, in which the entire procedure was determined with electrochemical techniques, such as EIS and cyclic voltammetry (CV). As shown in Fig. 2a, the EIS Nyquist plots of the Tb-MOF-on-Fe-MOF-based aptasensor for detection of CA125 were determined and simulated with an equivalent circuit (Fig. S1 inset). In fact, the variation in electrochemical activity of the electrode surface can be represented by its simulated R_{ct} value (Yu et al., 2010). As such, the R_{ct} value of bare AE is small (165.6 Ω), due to its excellent electrochemical conductivity (Zhou et al., 2017). The Tb-MOF-on-Fe-MOF coated on AE surface increased the R_{ct} value of electrode to 429.4 Ω,

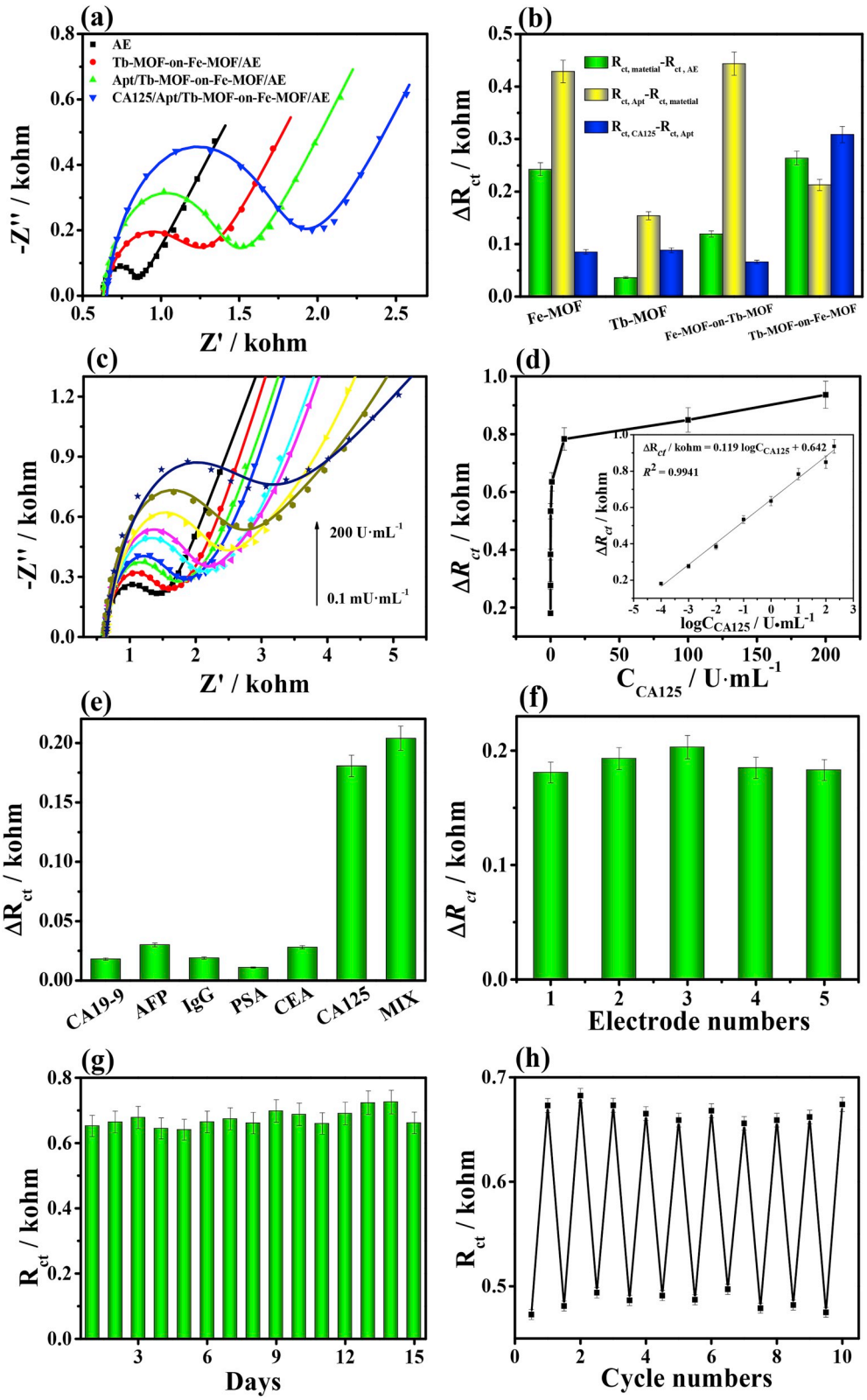

Fig. 2. EIS Nyquist plots of AEs modified with (a) Tb-MOF-on-Fe-MOF and (b) Fe-MOF-on-Tb-MOF AEs for detecting CA125, including the modification of AE with the bimetallic MOFs, the probe DNA immobilization, and the detection of CA125. (c) Variations in R_{ct} for each stage in the fabrication procedure of different MOFs-based aptasensors for detection of CA125. (c) EIS Nyquist plots for detection of CA125 at different concentrations (0, 0.0001, 0.001, 0.01, 0.1, 1, 10, 100, and 200 U mL^{-1}) using Tb-MOF-on-Fe-MOF-based aptasensor; (d) the calibration curves between ΔR_{ct} and CA125 concentrations (inset: the linear fit plot of ΔR_{ct} as function of the logarithm of CA125 concentration, the error bars are standard deviations for $n = 3$). (e) Selectivity, (f) reproducibility, (g) stability, and (h) regenerability of the proposed aptasensor for detection of CA125 ($n = 3$).

indicating a weaker electrochemical conductivity of the Tb-MOF-on-Fe-MOF layer which prevented electron transfer at the interface between electrolyte solution and electrode. Also, the R_{ct} value of Apt/Tb-MOF-on-Fe-MOF/AE continuously increased to 642.3 Ω when aptamer strands were anchored on surface of Tb-MOF-on-Fe-MOF, suggesting a successful immobilization of aptamer strands. The aptamer strands are possible to anchor over the surface of Tb-MOF-on-Fe-MOF-modified electrode by hydrogen bonding between the carboxyl groups of organic linkers and the phosphate groups of aptamers (Sun et al., 2017). The phosphate groups of anchored aptamer strands ionized into negative charges in water solution, which caused the repulsive interactions with $[Fe(CN)_6]^{3-/4-}$ ions. The difficulty of electron transfer at the interface resulted in the increase of R_{ct} value (Zhou et al., 2019b). The formation of G-quadruplex between aptamer strands and CA125 at the interface

continuously hampered the electron transfer due to presence of CA125 (Nie et al., 2018), leading to the increase of R_{ct} value.

The entire detection for CA125 with Tb-MOF-on-Fe-MOF-based aptasensor was studied by CV (Fig. S8a) using a redox probe (0.01 M PBS with 5 mM $Fe(CN)_6^{3-/4-}$), where similar result was obtained. After modification of AE by Tb-MOF-on-Fe-MOF, a considerable decrease in anodic and cathodic peak currents of the redox probe combined with increasing peak potential separation (ΔE_p) was observed, due to the relatively poor electrochemical activity of Tb-MOF-on-Fe-MOF. After the incubation of aptamer at Tb-MOF-on-Fe-MOF/AE surface, a continuous decrease of peak currents combined with increasing peak potential separation was observed, due to the increase of charge transfer resistance caused by the formation of a layer with highly packed negative charges at the electrode surface. This condition blocked the electron transfer and successful attachment of aptamer to Tb-MOF-on-Fe-MOF as an effective procedure for the construction of biosensor. The constructed biosensor was incubated in the CA125 solution. The decrease of peak current and increase of ΔE_p resulted from the binding of aptamer with CA125, which prevented the electron transfer at solid-liquid interface. The detection of CA125 was also conducted by CV using other aptasensors (Figs. S8b–d), based on Fe-MOF, Tb-MOF, and Fe-MOF-on-Tb-MOF, which showed similar trends with those of the Tb-MOF-on-Fe-MOF-based aptasensor. Notably, the charge transfer resistance in EIS data were changed with more sensitivity (Zamfir et al., 2011) compared with the peak current variations in CV. Consequently, EIS was used in subsequent measurements due to its acceptable sensitivity for CA125 detection.

Fe-MOF-, Tb-MOF-, and Fe-MOF-on-Tb-MOF-based aptasensors were similarly fabricated to detect CA125 and measured by EIS (Fig. S9). The EIS data also showed similar trends with those of Tb-MOF-on-Fe-MOF-based aptasensor. All simulated R_{ct} values of four kinds of aptasensors were summarized in Table S1. The calculated R_{ct} values of electrodes increased with the order of the modification of bare AE with different MOFs, aptamer immobilization, and detection of CA125. In fact, the difference of R_{ct} values caused by each step can represent the loading amount of the added layer (Liu et al., 2019). Therefore, the sensing performances of the four kinds of aptasensors were assessed based on the relative changes in their R_{ct} values of each step (Zhou et al., 2019), that is, the difference in R_{ct} values (ΔR_{ct}) before and after the new layer coating ($\Delta R_{ct} = R_{ct,i+1} - R_{ct,i}$) (Fig. 2b). For the Fe-MOF-based aptasensor, the modification of Fe-MOF on bare AE led to the largest increase of R_{ct} value (242.7 Ω), indicating the lowest electrochemical conductivity of Fe-MOF. On the contrary, the Tb-MOF modified electrode exhibited the smallest change in R_{ct} values (36.2 Ω), indicating its superior electrochemical activity to Fe-MOF. Thus, the presence of Tb-MOF enhanced the electron transfer at solid-liquid interface. As a result, a completely different behavior of aptamer immobilization was obtained for the two aptasensors. The aptamer immobilization on Fe-MOF/AE (Apt/Fe-MOF/AE) caused a large variation of R_{ct} (428.9 Ω). However, only a small R_{ct} difference of CA125/Apt/Fe-MOF/AE was obtained (85.2 Ω) in detection of CA125. In comparison, a smaller ΔR_{ct} caused by aptamer anchoring over Tb-MOF/AE was observed (154.0 Ω). Interestingly, a comparable ΔR_{ct} (88.5 Ω) was obtained in detection of CA125 using the Tb-MOF-based aptasensor. Although abundant aptamer strands were anchored on Fe-MOF electrode, most of the formed G-quadruplexes were removed from the platform, affording poor stability. By contrast, the G-quadruplex demonstrated high stability for Tb-MOF-based aptasensor, suggesting that Tb-MOF exhibited stronger binding interaction with the formed complex. The results were similar to our previous work (Zhou et al., 2019a). As reported (Guo et al., 2017), aptamer strands can immobilize over the MOF surface and also penetrate into the cavities of MOFs. The pore size of Fe-MOF is 1.68 $cm^3\,g^{-1}$ (Zhang et al., 2016), which is larger than that of Tb-MOF of 0.31 $cm^3\,g^{-1}$ (Jiang et al., 2010). Considerable aptamer strands anchored on Fe-MOF due to its large pore size via complicated interactions, such as $\pi-\pi^*$ stacking, hydrogen bonds between organic ligands and aptamer strands, coordination forces between metal ions and backbone of aptamer strands, and electrostatic forces (Urbanová et al., 2018). However, the strong interactions between aptamer and CA125 removed the formed G-quadruplex from Fe-MOF due to the long sequence of the CA125 aptamer strand (57 mer). As for Tb-MOF, the aptamer strand tightly anchored over its surface via the formation of G-Tb^{3+}-G complex, due to the coordination forces of Tb^{3+} with G base of aptamer strands (Wu et al., 2017). That is to say, Tb-MOF stabilized the G-quadruplex of aptamer and CA125. As a consequence, a novel CA125 aptasensor with prominent sensing performance can be developed by combining Fe-MOF with Tb-MOF.

The MOF-on-MOF strategy was applied to fabricate the platforms for CA125 detection. As shown in Fig. 2b, Fe-MOF-on-Tb-MOF- and Tb-MOF-on-Fe-MOF-based aptasensors exhibited substantially different sensing behaviors towards CA125. As for Fe-MOF-on-Tb-MOF-based aptasensor, although the Tb-MOF interior layer enhanced the electrochemical activity with small ΔR_{ct} of 119.3 Ω and the outer layer of Fe-MOF resulted in large amounts of aptamer strands to immobilize on the electrode with large ΔR_{ct} of 443.7 Ω, few G-quadruplexes were reserved after the combination of aptamer strands with CA125, giving a small ΔR_{ct} of 66.1 Ω. For Tb-MOF-on-Fe-MOF-based aptasensor, the ΔR_{ct} values caused by modification of Tb-MOF-on-Fe-MOF and aptamer immobilization were 263.8 and 212.9 Ω. The Tb-MOF-on-Fe-MOF electrode exhibited poorer electrochemical activity compared with Tb-MOF and less aptamer immobilization compared with Fe-MOF-based aptasensor. The detection of CA125 by Tb-MOF-on-Fe-MOF-based aptasensor gave a large ΔR_{ct} value of 308.7 Ω. All these results confirm that Tb-MOF-on-Fe-MOF-based aptasensor demonstrated superior sensing performances compare with other aptasensors. Additionally, the difference in the surface morphology of the Tb-MOF-on-Fe-MOF was investigated by SEM, as shown in Fig. S10. The results reveal that both the nanostructures of Apt/Tb-MOF-on-Fe-MOF and CA125/Apt/Tb-MOF-on-Fe-MOF retain the original irregular structure of Tb-MOF-on-Fe-MOF. It hints that the immobilization of aptamer strands and binding of CA 125 would not affect the surface morphology of Tb-MOF-on-Fe-MOF.

To achieve the suitable determination parameters for detection of CA125 using Tb-MOF-on-Fe-MOF-based aptasensor, the influence of Tb-MOF-on-Fe-MOF dosage, aptamer concentration, and binding time of CA125 on the sensing performances was investigated (**Supplementary Material S5**, Fig. S11, **S12** and **S13**). The electrochemical results revealed that the suitable testing parameters are 1.0 $mg{\cdot}mL^{-1}$ for Tb-MOF-on-Fe-MOF, 100 nM for aptamer solution, and 50 min for binding time towards CA125 detection in the present work.

3.3. Sensing performances of Tb-MOF-on-Fe-MOF-based aptasensor for CA125 detection

The LOD and dynamic range of developed Tb-MOF-on-Fe-MOF-based aptasensor were estimated by EIS for detection of targeted CA125 at different concentrations. As depicted in Fig. 2c, typical Nyquist plots of the fabricated aptasensor before and after incubation with different concentrations of CA125 solutions were recorded. The ΔR_{ct} value depended on the concentration of CA125, where the ΔR_{ct} value increased with the increase of CA125 concentration. The calibration plot of CA125 concentration versus ΔR_{ct} (the difference of impedance before and after incubation with CA125) demonstrated a linear dynamic range from 0.1 $mU{\cdot}mL^{-1}$ to 200 $U{\cdot}mL^{-1}$ with an R^2 of 0.9941. The ΔR_{ct} value began to level off when CA125 concentration was larger than 10 $U{\cdot}mL^{-1}$, suggesting the saturated binding of aptamer strands and CA125. Thus, the determination behavior of CA125 with the proposed Tb-MOF-on-Fe-MOF-based aptasensor abided the Langmuir-Freundlich isotherm (Thapa et al., 2017). The LOD was graphically calculated from the calibration plot with the steep slope encompassing the first four data points (Fig. 2d). On the basis of IUPAC, LOD was calculated to be 58 $\mu U{\cdot}mL^{-1}$ by using the following equation:

Table 1
Comparison of the proposed and reported biosensors for detection of CA125.

Materials	Detection method	Detection range ($U{\cdot}mL^{-1}$)	LOD ($U{\cdot}mL^{-1}$)	Refs.
CdTe790 nanocrystals	Electrochemiluminescence -multiplexing immunoassay	0.005 − 1	0.001	Zhang et al. (2018b)
Microfluidic origami device	Electrochemiluminescence	0.01 − 100	0.0074	Wang et al. (2013)
Chitosan-gold nanoparticle/multiwall carbon nanotube/graphene oxide	Chronoamperometry	0.01 − 100	0.002	Samadi Pakchin et al. (2018)
Phosphoserine imprinted CNT nanosensor	Fluorescence	3.125 − 150	0.492	Büyüktiryaki et al. (2017)
Multi-functionalized g-C_3N_4	Electrochemiluminescence	0.001 − 5	0.0004	Wu et al. (2016)
Gold nanostructure	DPV	10 − 100	5.5	Torati et al. (2017)
Mercaptopropionic acid/AuNP@SiO_2/CdSe QD	EIS	0 − 0.1	0.0016	Johari-Ahar et al. (2015)
Tb-MOF-on-Fe-MOF	**EIS**	**0.0001-200**	**0.000058**	**This work**

$$LOD = 3S_b/m$$

in which S_b refers to the standard deviation, and m is the slope referred to the gradient of calibration graph. The proposed aptasensor exhibited low LOD and high sensitivity compared with other reported biosensors used for the determination of CA125 (Table 1). The excellent sensing performances of the Tb-MOF-on-Fe-MOF-based aptasensor can be attributed to the following points: (i) large amount of anchored aptamer strands for the strong bioaffinity of Fe-MOF, (ii) good electrochemical activity of Tb-MOF, and (iii) high stabilizing ability of G-quadruplex complex formed between aptamer strands and CA125 due to the synergistic effect between Fe-MOF and Tb-MOF.

3.4. Specificity, reproducibility, stability, and regenerability of aptasensor

The specificity of Tb-MOF-on-Fe-MOF-based aptasensor was confirmed through EIS under different interferents, including CA19-9, AFP, IgG, PSA, CEA, and mixture of these interferents with CA125 (Fig. 2e). No substantial EIS response was obtained from the interferents, whereas a high EIS response was due to CA125 and the mixture of interferents. This result revealed the good selectivity of the proposed electrochemical aptasensor toward CA125, due to the excellent specific affinity of aptamer strands and CA125, which was not disturbed by other possible cancer markers.

The reproducibility of the proposed aptasensor was assessed independently using five Tb-MOF-on-Fe-MOF-based aptasensors under the same conditions. As shown in Fig. 2f, an acceptable reproducibility was achieved. Moreover, the storage stability of Tb-MOF-on-Fe-MOF-based aptasensor was explored for 15 days (Fig. 2g). The final detection signals preserved 101.4% of the initial response for detection of CA125 (0.1 $mU{\cdot}mL^{-1}$) using the same aptasensor mode, illustrating its good storage stability. The regenerability of Tb-MOF-on-Fe-MOF-based aptasensor was validated by immersing CA125/Apt/Tb-MOF-on-Fe-MOF/AE into 1.0 M NaOH at 4 °C for 2 min to dissociate CA125 with the aptamer strands, followed by rinsing with massive Milli-Q water. As such, the developed aptasensor could be regenerated. Subsequently, the regenerated Apt/Tb-MOF-on-Fe-MOF/AE was incubated with CA125 solution (0.1 $mU{\cdot}mL^{-1}$). The detection of CA125 was repeated 10 times and the recorded EIS responses were shown in Fig. 2h. No palpable variation was observed in R_{ct} values of the developed aptasensor. This condition implied that Tb-MOF-on-Fe-MOF-based aptasensor can be easily regenerated in NaOH solution without loss of the determination signal.

3.5. Detection of living MCF-7 cells using Tb-MOF-on-Fe-MOF-based aptasensor

To evaluate whether the as-prepared bimetallic TbFe-MOFs could be used as the platforms for direct detection of living cancer cells, their cell viability was determined by incubating MCF-7 cell lines in vitro. As depicted in Fig. S14a, the cytotoxicity of Tb-MOF-on-Fe-MOF slightly declined after 24 h, indicating that 90% of MCF-7 cells were still alive with the Tb-MOF-on-Fe-MOF concentration of 100 $\mu g{\cdot}mL^{-1}$. Consequently, the as-obtained Tb-MOF-on-Fe-MOF showed good biocompatibility towards MCF-7 cells, revealing its suitability as the platform for detecting living cells. Meanwhile, the cell uptake of Tb-MOF-on-Fe-MOF was evaluated by incubating MCF-7 cells into the Tb-MOF-on-Fe-MOF suspension and surveyed through a confocal laser scanning microscopy. As illustrated in Fig. S14b, weak green fluorescence appeared after MCF-7 cells adsorbed with Tb-MOF-on-Fe-MOF were excited by 400 nm laser, due to the fluorescent properties of Tb-MOF-on-Fe-MOF. The merged photo revealed that Tb-MOF-on-Fe-MOF could preferentially accumulate in cancer cells and directly exhibit fluorescence without requiring the use of other dyes. This result indicated that Tb-MOF-on-Fe-MOF NPs can be endocytosed by cancer cells.

The good biocompatibility and cell endocytosis of Tb-MOF-on-Fe-MOF revealed its suitability as the platform for direct detection of living cancer cells. The developed aptasensor was used to detect MCF-7 cells, and the entire procedure was evaluated by EIS and CV. As displayed in Fig. 3a, the Nyquist curve of Tb-MOF-on-Fe-MOF/AE provided a R_{ct} of 454.9 Ω. After aptamer immobilization, the R_{ct} value increased to 632.1 Ω, due to the blocking effect of anchored aptamers over electrode surface. The R_{ct} value continuously increased to 700.6 Ω when the proposed aptasensor was used to detect MCF-7 cells. This result showed the biorecognition between CA125 aptamer and MCF-7 cells. Similar result was also obtained for CV measurements (Fig. 3b). To validate the specificity of the proposed aptasensor for detecting cancer cells, the same aptasensor was used to determine the normal L929 cells under the same measurement conditions. As displayed in Fig. S15, the EIS results demonstrate that no substantial variation was observed after the detection of L929 cells, giving a low variation of R_{ct} (40 Ω). Thus, the aptasensor exhibited high specificity towards cancer cells.

To validate the detection sensitivity of the proposed aptamer towards cancer cells, MCF-7 cells with diverse concentrations were applied to assess the analytical performances of Tb-MOF-on-Fe-MOF-based biosensor. The ΔR_{ct} value ($\Delta R_{ct} = R_{ct,\ \text{MCF-7}} - R_{ct,\ \text{Apt}}$) significantly increased with the concentration increase of MCF-7 cells from 0 to 10^5 $cell{\cdot}mL^{-1}$ (Fig. 3c). Fig. 3d reveals a good liner relationship between ΔR_{ct} value and the logarithms of the concentrations of MCF-7 cells within the range from 100 to 10^5 $cell{\cdot}mL^{-1}$. According to the IUPAC method, the LOD could be calculated to 19 $cells{\cdot}mL^{-1}$. Here, three measurements were conducted in parallel to obtain an average value. Our present approach provided a lower LOD and a wider linear detection range of the proposed sensor towards MCF-7 cells, by comparing its sensing performances with other reported biosensors (Table 2). Apart from the ultralow LOD for detection of MCF-7 cells, the reproducibility and stability of the developed aptasensor towards MCF-7 cells were also explored. The reproducibility of Tb-MOF-on-Fe-MOF-based aptasensor was evaluated using the same Tb-MOF-on-Fe-MOF through five repeated tests with different cell concentrations (Fig. 3e), i.e. 500, 5000, and 100000 cell mL^{-1}. The EIS responses displayed relatively consistent values, affording a relative standard deviation

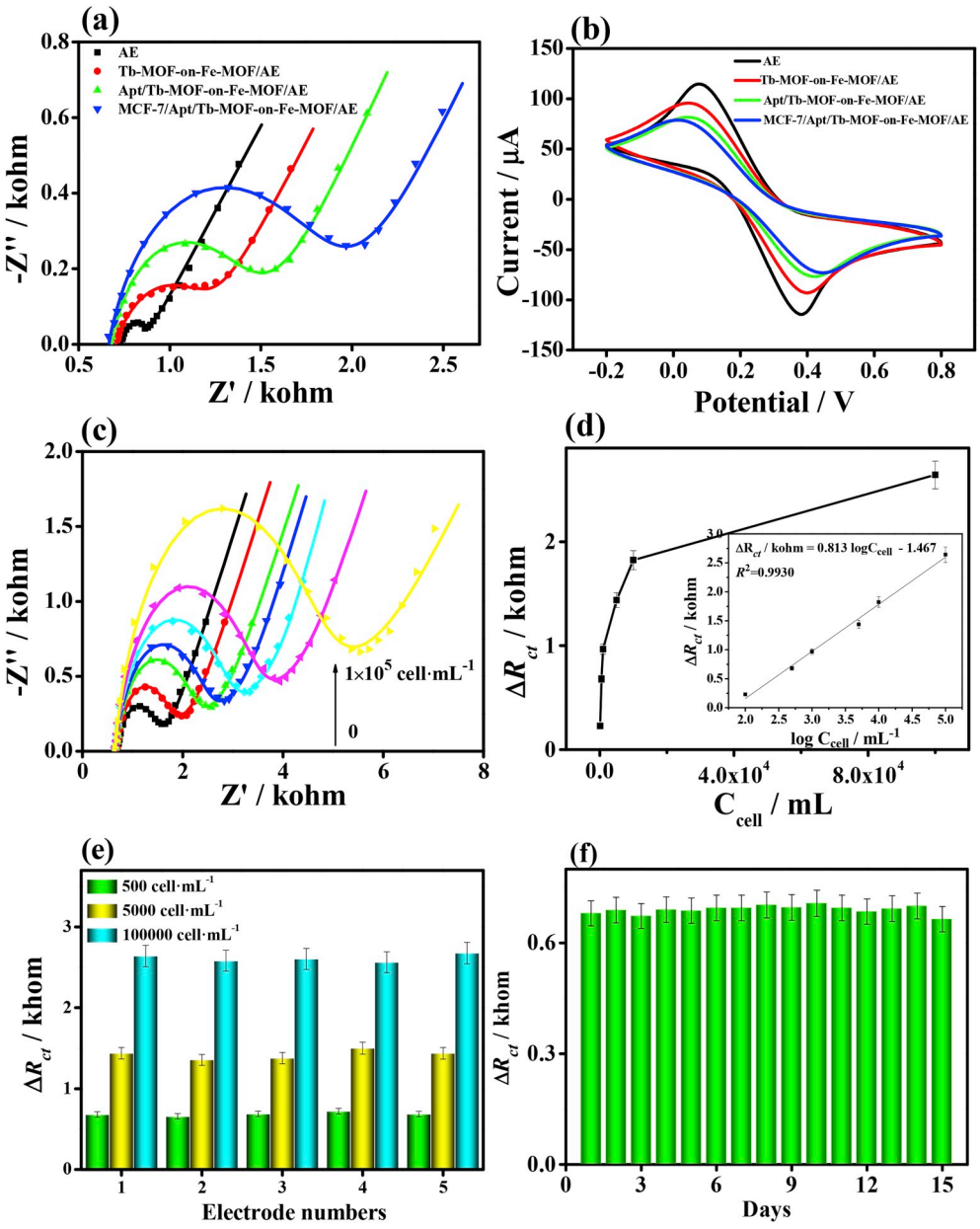

Fig. 3. (a) EIS Nyquist and (b) CV curves of Tb-MOF-on-Fe-MOF modified AEs for detection of MCF-7 cells in 0.01 M PBS (pH 7.4) with 5.0 mM $[Fe(CN)_6]^{3-/4-}$ redox. (c) EIS responses of Tb-MOF-on-Fe-MOF-based aptasensor at different MCF-7 cells concentrations (0, 100, 500, 1000, 5000, 10000, and 100000 cell·mL^{-1}). (d) Dependence of ΔR_{ct} on the concentration of MCF-7 cells (inset: the linear parts of calibration curves, $n = 3$). (e) The reproducibility of proposed aptasensor for MCF-7 cells detection at different concentrations (500, 5000 and 100000 cell·mL^{-1}). (f) The stability of proposed aptasensor for MCF-7 cells detection (500 cell·mL^{-1}) within 15 days.

(RSD) of 3.31, 3.98 and 1.76%, revealing its excellent sensing reproducibility. The stability of Tb-MOF-on-Fe-MOF-based aptasensor towards MCF-7 cells was confirmed for 15 days (Fig. 3f). The final EIS response was obtained as 97.7% of the initial response for detection of 500 cell·mL^{-1} using the same aptasensor mode, indicating its good stability. Therefore, the proposed Tb-MOF-on-Fe-MOF-based biosensor could be utilized in detection of both cancer marker CA125 and the living cancer cells due to its good biocompatibility and endocytosis.

3.6. Detection capability in serum samples

The reliability and feasibility of the proposed aptasensor in real serum were also investigated by adding CA125 or MCF-7 cells with various concentrations to the human serum, which were pretreated and diluted for 500 times. The determination procedure was measured by EIS and analyzed based on the calibration curve shown in the inset of Figs. 2d and 3d. All recoveries listed in Tables S2 and S3 confirmed that

Table 2
Comparison of the proposed and reported biosensors for living MCF-7 cells detection.

Materials	Detection method	Detection range (cell·mL^{-1})	LOD (cell·mL^{-1})	Refs.
ZrHf-MOF	EIS	$1 \times 10^2 - 1 \times 10^5$	23	Gu et al. (2019)
Montmorillonite-human serum albumin based composite	EIS	$1.5 \times 10^2 - 7.5 \times 10^6$	148	Yaman et al. (2019)
NiO nanoparticles	SPR	$5 \times 10^2 - 4 \times 10^3$	136	Jia et al. (2016)
Au nanoparticles/ three-dimensional reduced graphene oxide	DPV	$50–1 \times 10^7$	20	Wang et al. (2018b)
TiO_2/CdTe heterostructure	Photoelectrochemical	$1 \times 10^3 - 1 \times 10^5$	400	Wang et al. (2016)
Au nanocages/ amino-functionalized multiwalled carbon nanotubes	EIS	$1 \times 10^2 - 1 \times 10^6$	80	Yang et al. (2018)
Tb-MOF-on-Fe-MOF	**EIS**	$\mathbf{1 \times 10^2 - 1 \times 10^5}$	**19**	**This work**

Tb-MOF-on-Fe-MOF-based aptasensor could achieve good performances for CA125 and MCF-7 cells detection in serum samples, showing the RSD of 1.50%-4.64% and 2.48%-3.76%, respectively. Therefore, the proposed strategy and developed aptasensor showed high accuracy for practical applications.

4. Conclusion

In this study, we designed and synthesized a novel kind of bimetallic TbFe-MOF nanostructures constructed with MOF-on-MOF strategy and used them as platforms to anchor CA125 aptamers for simultaneously detecting CA125 and living MCF-7 cells. Considering the intrinsic features of individual components, including electrochemical activity, fluorescence and large pore size of Tb-MOF as well as strong binding affinity to aptamers and biocompatibility of Fe-MOF, Tb-MOF-on-Fe-MOF-based aptasensor showed higher stability of the formed G-quadruplex between aptamer and CA125 and superior sensing performance compared with other aptasensors. That is, the change of construction strategies of bimetallic MOFs can lead to various sensing behaviors. The final optimized Tb-MOF-on-Fe-MOF-based aptasensor showed LODs of 58 $\mu U \cdot mL^{-1}$ and 19 $cell \cdot mL^{-1}$ towards CA125 and MCF-7 cells, respectively, with good selectivity, stability, reproducibility and acceptable applicability. Although the developed strategy provided promising applications of MOFs in biosensing fields, their practical applications should be investigated in the future using real-time clinical specimens.

Declarations of interest

None.

CRediT authorship contribution statement

Minghua Wang: Validation, Formal analysis, Writing - original draft. **Mengyao Hu:** Validation, Formal analysis, Writing - original draft. **Zhenzhen Li:** Validation, Formal analysis. **Linghao He:** Formal analysis, Investigation. **Yingpan Song:** Methodology, Formal analysis. **Qiaojuan Jia:** Validation, Formal analysis. **Zhihong Zhang:** Conceptualization, Writing - review & editing, Supervision. **Miao Du:** Writing - review & editing, Supervision.

Acknowledgements

This work was financially supported by the National Natural Science Foundation of China (Nos. U1604127 and 21571158) and the Key Research Project of University of Henan Province, China (No. 19zx004).

Appendix A. Supplementary data

Supplementary data to this article can be found online at https://doi.org/10.1016/j.bios.2019.111536.

References

Alizadeh, N., Hallaj, R., Salimi, A., 2017. Biosens. Bioelectron. 94, 184–192.
Aycla, Y., Ketul, C.P., John, C.A., Tejal, A.D., John, H., Nabil, C., Brent, E.L., Oliver, K., Vien, V., Sai, C., David, G., Matthew, A., S.U, M., Bennett, B.G., 2006. Ieee J. Sel. Top. Quant. 12, 148–155.
Büyüktiryaki, S., Say, R., Denizli, A., Ersöz, A., 2017. Talanta 167, 172–180.
Chang, Z., Yang, D., Xu, J., Hu, T., Bu, X., 2015. Adv. Mater. 27, 5432–5441.
Choi, S., Kim, T., Ji, H., Lee, H.J., Oh, M., 2016. J. Am. Chem. Soc. 138, 14434–14440.
Cramer, D.W., Fichorova, R.N., Terry, K.L., Yamamoto, H., Vitonis, A.F., Ardanaz, E., Aune, D., Boeing, H., Brändstedt, J., Boutron-Ruault, M., Chirlaque, M., Dorronsoro, M., Dossus, L., Duell, E.J., Gram, I.T., Gunter, M., Hansen, L., Idahl, A., Johnson, T., Khaw, K., Krogh, V., Kvaskoff, M., Mattiello, A., Matullo, G., Merritt, M.A., Nodin, B., Orfanos, P., Onland-Moret, N.C., Palli, D., Peppa, E., Quirós, J.R., Sánchez-Perez, M., Severi, G., Tjønneland, A., Travis, R.C., Trichopoulou, A., Tumino, R., Weiderpass, E., Fortner, R.T., Kaaks, R., 2018. Cancer Epidem. Biomar. 27, 790–804.
Deng, K., Liu, X., Li, C., Huang, H., 2018. Biosens. Bioelectron. 117, 168–174.
Deng, K., Liu, X., Li, C., Hou, Z., Huang, H., 2017. Sens. Actuators B Chem. 253, 1–9.
Du, M., Li, C., Liu, C., Fang, S., 2013. Coord. Chem. Rev. 257, 1282–1305.
Feng, L., Yuan, S., Li, J., Wang, K., Day, G.S., Zhang, P., Wang, Y., Zhou, H., 2018. ACS Cent. Sci. 4, 1719–1726.
Gedi, V., Song, C.K., Kim, G.B., Lee, J.O., Oh, E., Shin, B.S., Jung, M., Shim, J., Lee, H., Kim, Y., 2018. Sens. Actuators B Chem. 256, 89–97.
Gu, C., Guo, C., Li, Z., Wang, M., Zhou, N., He, L., Zhang, Z., Du, M., 2019. Biosens. Bioelectron. 134, 8–15.
Gu, Y., Wu, Y., Li, L., Chen, W., Li, F., Kitagawa, S., 2017. Angew. Chem. Int. Ed. 56, 15658–15662.
Guo, C., Su, F., Song, Y., Hu, B., Wang, M., He, L., Peng, D., Zhang, Z., 2017. ACS Appl. Mater. Interfaces 9, 41188–41199.
He, X., Tian, H., 2016. Small 12, 144–160.
Jalalian, S.H., Karimabadi, N., Ramezani, M., Abnous, K., Taghdisi, S.M., 2018. Trends Food Sci. Technol. 73, 45–57.
Jia, S., Li, P., Koh, K., Chen, H., 2016. Microchim. Acta 183, 683–688.
Jiang, H., Tsumori, N., Xu, Q., 2010. Inorg. Chem. 49, 10001–10006.
Johari-Ahar, M., Rashidi, M.R., Barar, J., Aghaie, M., Mohammadnejad, D., Ramazani, A., Karami, P., Coukos, G., Omidi, Y., 2015. Nanoscale 7, 3768–3779.
Lee, S.R., Park, H.B., Kim, K.H., 2018. Anal. Chem. 90, 13212–13216.
Li, N., Jiang, H., Wang, X., Wang, X., Xu, G., Zhang, B., Wang, L., Zhao, R., Lin, J., 2018a. Trac. Trends Anal. Chem. 102, 60–74.
Li, S., Huo, F., 2015. Nanoscale 7, 7482–7501.
Li, Y., Yu, C., Yang, B., Liu, Z., Xia, P., Wang, Q., 2018b. Biosens. Bioelectron. 102, 307–315.
Liu, C., Zhang, Z., Chen, M., Zhao, H., Duan, F., Chen, D., Wang, M., Zhang, S., Du, M., 2017. Chem. Commun. 53, 3941–3944.
Liu, R., Ran, L., Niu, B., Wei, Y., 2018. J. Nanosci. Nanotechnol. 18, 4667–4674.
Liu, X., Hu, M., Wang, M., Song, Y., Zhou, N., He, L., Zhang, Z., 2019. Biosens. Bioelectron. 123, 59–68.
Lu, M., Deng, Y., Luo, Y., Lv, J., Li, T., Xu, J., Chen, S., Wang, J., 2019. Anal. Chem. 91, 888–895.
Mendonsa, S.D., Bowser, M.T., 2005. J. Am. Chem. Soc. 127, 9382–9383.
Meng, H., Liu, H., Kuai, H., Peng, R., Mo, L., Zhang, X., 2016. Chem. Soc. Rev. 45, 2583–2602.
Mi, L., Ding, Q., Chen, W., Zhao, L., Hou, H., Liu, C., Shen, C., Zheng, Z., 2013. Dalton Trans. 42, 5724–5730.
Nie, Y., Yang, M., Ding, Y., 2018. Microchim. Acta 185, 331.
Qiao, X., Xia, F., Tian, D., Chen, P., Liu, J., Gu, J., Zhou, C., 2019. Anal. Chim. Acta 1050, 51–59.
Qu, F., Sun, C., Lv, X., You, J., 2018. Microchim. Acta 185, 359.
Razmi, N., Hasanzadeh, M., 2018. Trac. Trends Anal. Chem. 108, 1–12.
Samadi Pakchin, P., Ghanbari, H., Saber, R., Omidi, Y., 2018. Biosens. Bioelectron. 122, 68–74.
Song, Y., Duan, F., Zhang, S., Tian, J., Zhang, Z., Wang, Z., Liu, C., Xu, W., Du, M., 2017. J. Mater. Chem. A 5, 19378–19389.
Stoltenburg, R., Reinemann, C., Strehlitz, B., 2007. Biomol. Eng. 24, 381–403.
Su, F., Zhang, S., Ji, H., Zhao, H., Tian, J., Liu, C., Zhang, Z., Fang, S., Zhu, X., Du, M., 2017. ACS Sens. 2, 998–1005.
Sun, B., Zhao, H.Q., Xie, B.P., Bai, L.P., Jiang, Z.H., Chen, J.X., 2017. J. Inorg. Biochem. 176, 17–23.
Taghdisi, S.M., Danesh, N.M., Ramezani, M., Emrani, A.S., Abnous, K., 2016. Biosens. Bioelectron. 80, 532–537.
Thapa, A., Soares, A.C., Soares, J.C., Awan, I.T., Volpati, D., Melendez, M.E., Fregnani, J.H.T.G., Carvalho, A.L., Oliveira, O.N., 2017. ACS Appl. Mater. Interfaces 9, 25878–25886.
Torati, S.R., Kasturi, K.C.S.B., Lim, B., Kim, C., 2017. Sens. Actuators B Chem. 243, 64–71.
Törer, H., Aydın, E.B., Sezgintürk, M.K., 2018. Anal. Chim. Acta 1024, 65–72.
Trausch, J.J., Shank-Retzlaff, M., Verch, T., 2017. Vaccine 35, 5495–5502.
Urbanová, V., Jayaramulu, K., Schneemann, A., Kment, Š., Fischer, R.A., Zbořil, R., 2018. ACS Appl. Mater. Interfaces 10, 41089–41097.
Wang, H., Zhou, C., Sun, X., Jian, Y., Kong, Q., Cui, K., Ge, S., Yu, J., 2018b. Biosens. Bioelectron. 117, 651–658.
Wang, K., Zhang, R., Sun, N., Li, X., Wang, J., Cao, Y., Pei, R., 2016. ACS Appl. Mater. Interfaces 8, 25834–25839.
Wang, S., Ge, L., Yan, M., Yu, J., Song, X., Ge, S., Huang, J., 2013. Sens. Actuators B Chem. 176, 1–8.
Wang, S., Li, Z., Duan, F., Hu, B., He, L., Wang, M., Zhou, N., Jia, Q., Zhang, Z., 2019. Anal. Chim. Acta 1047, 150–162.
Wang, Z., Wannapaiboon, S., Rodewald, K., Tu, M., Rieger, B., Fischer, R.A., 2018a. J. Mater. Chem. A 6, 21295–21303.
Wei, H., Li, B., Li, J., Wang, E., Dong, S., 2007. Chem. Commun. 3735–3737.
Wu, K., Ma, C., Liu, H., He, H., Zeng, W., Wang, K., 2017. Anal. Methods-UK 9, 3055–3060.
Wu, L., Sha, Y., Li, W., Wang, S., Guo, Z., Zhou, J., Su, X., Jiang, X., 2016. Sens. Actuators B Chem. 226, 62–68.
Wu, S., Zhuang, G., Wei, J., Zhuang, Z., Yu, Y., 2018. J. Mater. Chem. A 6, 18234–18241.
Xu, S., Zhang, R., Zhao, W., Zhu, Y., Wei, W., Liu, X., Luo, J., 2017. Biosens. Bioelectron. 92, 570–576.
Yaman, Y.T., Akbal, O., Abaci, S., 2019. Biosens. Bioelectron. 132, 230–237.
Yang, Y., Fu, Y., Su, H., Mao, L., Chen, M., 2018. Biosens. Bioelectron. 122, 175–182.
Yin, Z., Wan, S., Yang, J., Kurmoo, M., Zeng, M., 2019. Coord. Chem. Rev. 378, 500–512.
Yu, F., Chen, S., Chen, Y., Li, H., Yang, L., Chen, Y., Yin, Y., 2010. J. Mol. Struct. 982, 152–161.
Zamfir, L., Geana, I., Bourigua, S., Rotariu, L., Bala, C., Errachid, A., Jaffrezic-Renault, N., 2011. Sens. Actuators B Chem. 159, 178–184.

Zhang, F., He, Y., Fu, K., Fu, L., Zhang, B., Wang, H., Zou, G., 2018b. Biosens. Bioelectron. 115, 77–82.
Zhang, L., Wang, J., Ren, X., Zhang, W., Zhang, T., Liu, X., Du, T., Li, T., Wang, J., 2018a. J. Mater. Chem. A 6, 21029–21038.
Zhang, Z., Ji, H., Song, Y., Zhang, S., Wang, M., Jia, C., Tian, J., He, L., Zhang, X., Liu, C., 2017. Biosens. Bioelectron. 94, 358–364.
Zhang, Z., Li, X., Liu, B., Zhao, Q., Chen, G., 2016. RSC Adv. 6, 4289–4295.
Zhou, F., Yao, Y., Luo, J., Zhang, X., Zhang, Y., Yin, D., Gao, F., Wang, P., 2017. Anal. Chim. Acta 969, 8–17.
Zhou, N., Ma, Y., Hu, B., He, L., Wang, S., Zhang, Z., Lu, S., 2019b. Biosens. Bioelectron. 127, 92–100.
Zhou, N., Su, F., Guo, C., He, L., Jia, Z., Wang, M., Jia, Q., Zhang, Z., Lu, S., 2019a. Biosens. Bioelectron. 123, 51–58.